



This is a repository copy of *Growth of BiFeO₃ thin films by chemical solution deposition: the role of electrodes.*

White Rose Research Online URL for this paper:
<http://eprints.whiterose.ac.uk/118529/>

Version: Accepted Version

Article:

Tomczk, M., Stroppa, D., Reaney, I.M. orcid.org/0000-0003-3893-6544 et al. (1 more author) (2017) Growth of BiFeO₃ thin films by chemical solution deposition: the role of electrodes. *Physical Chemistry Chemical Physics*, 19 (22). pp. 14337-14344. ISSN 1463-9076

<https://doi.org/10.1039/C7CP01842H>

Reuse

Items deposited in White Rose Research Online are protected by copyright, with all rights reserved unless indicated otherwise. They may be downloaded and/or printed for private study, or other acts as permitted by national copyright laws. The publisher or other rights holders may allow further reproduction and re-use of the full text version. This is indicated by the licence information on the White Rose Research Online record for the item.

Takedown

If you consider content in White Rose Research Online to be in breach of UK law, please notify us by emailing eprints@whiterose.ac.uk including the URL of the record and the reason for the withdrawal request.



eprints@whiterose.ac.uk
<https://eprints.whiterose.ac.uk/>

Growth of BiFeO₃ thin films by chemical solution deposition: the role of electrodes

Monika Tomczyk¹, Daniel G Stroppa², Ian M Reaney³, Paula M Vilarinho^{1*}

¹CICECO-Aveiro Institute of Materials, Department of Materials and Ceramic Engineering, University of Aveiro, 3810-193 Aveiro, Portugal

²INL- International Iberian Nanotechnology Laboratory, Av. Mestre José Veiga, 4715-330 Braga, Portugal.

³Department of Engineering Materials, University of Sheffield, Sheffield, S1 3JD, UK

* corresponding author, e-mail: paula.vilarinho@ua.pt

Abstract

BiFeO₃ (BFO) thin films were grown by chemical solution deposition on a range of electrodes to determine their role in controlling phase formation and microstructure. The crystallization on oxide electrodes followed the sequence: amorphous → Bi₂O₂(CO₃) → perovskite, while those on Pt crystallized directly from the amorphous phase. IrO₂ electrodes promoted perovskite phase formation at the lowest temperature and LaNiO₃ additionally induced local epitaxial growth. All compositions exhibited fully coherent Fe-rich precipitates within the grain interior of the perovskite matrix, whereas incoherent Bi₂Fe₄O₉ second phase was also observed at the grain boundaries of BFO grown on Pt electrodes. The latter could be observed by X-ray diffraction as well as transmission electron microscopy (TEM) but coherent precipitates were only observed by TEM, principally evidenced by their Z contrast in annular dark field images. These data have pronounced consequences for the extended use of BFO films under applied field for actuator, sensor and memory applications.

Introduction

In recent years, attention has been paid to materials possessing two or more of the following ferroic properties: ferroelasticity; ferroelectricity and (anti)ferromagnetism, a class of materials now referred to as multiferroics. Due to their potential technological applications in modern electronic devices, such as memory elements, sensors, and spintronics, they have become the

subject of intense research ¹. Rich in properties and functionality, bismuth ferrite (BiFeO_3 , BFO) has been studied more extensively than any other multiferroic, being hailed the most promising lead-free single phase multiferroic candidate for devices due to its intrinsic multiferroic nature above room temperature ². However, its compositional instability, often resulting in variation in functional properties is a major obstacle to full practical utilization ².

Early studies, dating back to the 1960's, pointed out the difficulties in the preparation of BFO free from non-perovskite, parasitic phases ³. Moreover, BFO exhibits high electrical conductivity, creating difficulties in applying large electric fields⁴. This high electrical conductivity is mainly attributed to the presence the Bi-rich sillenite type, $\text{Bi}_{25}\text{FeO}_{39}$ (or $\text{Bi}_{25}\text{FeO}_{40}$) phase and the Fe-rich mullite-type, $\text{Bi}_2\text{Fe}_4\text{O}_9$, and to defects in the crystal structure, such as oxygen vacancies originating from the reduction of Fe^{3+} to Fe^{2+} ⁵. Preparation of monophasic BiFeO_3 is extremely difficult due to the thermodynamics and kinetics of Bi_2O_3 – Fe_2O_3 system. Based on studies by Selbach et al. ⁶, $\text{Bi}_{25}\text{FeO}_{39}$ and $\text{Bi}_2\text{Fe}_4\text{O}_9$ phases are slightly more stable thermodynamically than BiFeO_3 in the temperature range 447 - 767°C. During the solid state reaction between Bi_2O_3 and Fe_2O_3 , $\text{Bi}_{25}\text{FeO}_{39}$ forms at the shell whereas a $\text{Bi}_2\text{Fe}_4\text{O}_9$ is formed at the reaction/diffusion front towards the iron oxide core. Once crystallized, $\text{Bi}_2\text{Fe}_4\text{O}_9$ is stable and consequently, the reaction is arrested so that BFO coexists with small amounts of $\text{Bi}_{25}\text{FeO}_{39}$ and $\text{Bi}_2\text{Fe}_4\text{O}_9$ ⁷. Furthermore, sublimation or evaporation of volatile Bi_2O_3 at elevated temperatures may also result in $\text{Bi}_2\text{Fe}_4\text{O}_9$ formation ⁸.

In contrast to bulk materials described above, the crystallization pathway to form thin films of BFO is quite different. BFO thin films have been grown via numerous methods including physical vacuum-based and chemical-based techniques but each deposition technique has drawbacks. BFO thin films grown by pulsed laser deposition (PLD) under incorrect oxygen pressures can develop parasitic iron oxide phases, such as α -type Fe_2O_3 or γ -type Fe_2O_3 ⁹ and in some cases nano-scale precipitation of $\text{Bi}_2\text{FeO}_{6-x}$, an Aurivillius compound ($n = 1$) with an orthorhombic crystal structure has been reported. More recently, using advanced transmission microscopy (TEM), the existence of a new Fe_2O_3 -rich perovskite nanophase, fully coherent with the matrix of Ti and Nd doped BiFeO_3 was reported with an approximate formula, $(\text{Fe}_{0.6}\text{Bi}_{0.25}\text{Nd}_{0.15})^{3+}\text{Fe}^{3+}\text{O}_3$ ¹⁰.

Similarly the preparation of monophasic BFO thin films by chemical solution deposition (CSD) requires accurate control of the processing parameters and Bi:Fe stoichiometry. Bi deficiency in the starting composition or from volatilization of Bi during the annealing steps leads to the formation of secondary phases and highly conductive films¹¹. To compensate for the Bi volatility, Bi excess is normally used in CSD BFO films. However, in the case of high Bi excess, phases such as Fe substituted α -Bi₂O₃ are formed at the BFO/Pt interface. Moreover, other common impurity phases such as: Bi₂O₃, Fe₂O₃, Bi₂Fe₄O₉, Bi₄₆Fe₂O₇₂ and Bi₂₄Fe₂O₃₉, have also been reported¹²⁻¹⁴. This broad spectrum of possible secondary phases in BFO thin films, sometimes difficult to detect by X-ray diffraction, due to their small particle size and volume fraction, determines the reproducibility of the electrical response.

The electrical properties of ferroelectric capacitors are not only affected by the intrinsic nature of the ferroelectric films but also by the electrodes due to differences in chemical nature, lattice parameter, work function and surface roughness¹⁵. The bottom electrode also serves as a template for growth and promotes phase stability¹⁵. Bottom electrodes for ferroelectric thin films can be either metal or oxide-based. The former group includes: platinum; iridium; ruthenium and copper, most commonly used due to their chemical and thermal stability. The latter group includes the rutile-type iridium (IrO₂) and ruthenium oxides (RuO₂) and perovskite-structured oxides, such as strontium ruthenate (SrRuO₃, SRO) and lanthanum nickelate (LaNiO₃, LNO). Among them, IrO₂ is easily and reproducibly deposited on Si substrates on a large scale at low cost¹⁶. Generally, Pt is used as a bottom and top electrode for thin film ferroelectric capacitors due to its high electrical conductivity, good stability at high temperatures and high Schottky barrier which lowers leakage current¹⁵ whereas SRO, IrO₂, RuO₂ and LNO have been reported to offer lattice matching, structural and chemical compatibility, a high diffusion barrier for oxygen, phase stability at high temperatures, and superior fatigue properties over Pt electrodes¹⁷. It is believed that oxygen vacancies in PZT thin films can easily be filled with oxygen from the oxide-based electrodes, resulting in a reduction in their build up at interfaces^{17, 18}. Oxide electrodes also have an important role in the processing of other lead-based and lead-free ferroelectric thin films. IrO₂ enhances the electrical performance of 0.37 BiScO₃-0.63 PbTiO₃¹⁹ and LNO interlayers promote (001) texture and improve the dielectric properties of Ba_{0.5}Sr_{0.5}TiO₃²⁰.

The use of oxide electrodes for fabrication of BFO thin films has to date been mainly limited to epitaxial thin films grown on SRO²¹ with only a few reports describing BFO films grown on oxide electrodes such as LNO and IrO₂. LNO and IrO₂ electrodes were studied for La and Nb co-doped BFO (BLNF) thin films fabricated by PLD. BLNF films on LNO/Si substrates showed strong (012) texture due to the lattice matching between BLNF (012) and LNO (001) whereas no preferred orientation was observed for IrO₂/Si. Moreover, BLNF films using LNO as the bottom electrode showed well-saturated ferroelectric loops with large remanent polarization, but poor fatigue resistance. BLNF thin films using IrO₂ as the bottom electrode displayed ferroelectric loops with high leakage current, but better fatigue resistance²². Comparative studies between Pt and LNO electrode for BFO films produced by RF-sputtering showed that LNO reduces crystallization temperature and improves the crystallinity of BFO films. Moreover, the electrical conductivity is greatly reduced due to improvements in the film/electrode interface, chemical homogeneity and surface roughness of the BFO on LNO interlayer²³. The reduction of electrical conductivity in BFO films prepared by CSD was also suggested to originate from the absence of parasitic phases and better quality of film/electrode interface, due to the use of LNO as bottom electrode but no preferred orientation was reported²⁴. Although, oxide electrodes such as LNO have been shown to improve crystallinity and chemical homogeneity of BFO, reduce the crystallization temperature and induce texture and improve film/electrode interfaces in BFO thin films, the microstructure and phase formation have not been addressed.

In this paper, we use annular dark field (ADF) scanning transmission electron microscopy (STEM), high resolution TEM, energy dispersive X-ray spectroscopy (EDX) complemented by grazing incident XRD to identify the crystallization pathway and microstructure of BFO films prepared by a chemical solution deposition route on Pt/TiO₂/SiO₂/(100)Si, LNO/Pt/TiO₂/SiO₂/(100)Si and IrO₂/TiO₂/SiO₂/(100)Si electrodes.

Experimental Section

Lanthanum nitrate hexahydrate (La(NO₃)₃ · 6H₂O, Merck, 99%) and nickel (II) nitrate hexahydrate (Ni(NO₃)₂ · 6H₂O, Fluka, 98.5%) were dissolved in 5 ml of deionized water, and mixed in the stoichiometric ratio of La:Ni=1:1. To improve the solution wettability and avoid film cracking during heating, 1 ml of formamide (Merck, 99.5%) was used. Finally, ethanol

absolute (Merck, 99.8%) was added until the resultant concentration of LNO solution was diluted to 0.2 M. The LNO films were deposited by spin-coating (KW-4A Spin Coater) the solution on Pt/TiO₂/SiO₂/Si substrates at 2500 rpm for 45 s and annealed by rapid thermal processing (Qualiflow JetFirst 100) at 700 °C for 5 min in O₂ atmosphere.

BFO precursor solutions were prepared using bismuth nitrate (Bi(NO₃)₃·5H₂O, Sigma Aldrich, 99.99%) and iron acetylacetonate (Fe(CH₃COCHCOCH₃)₃, ABCR, 99%). Acetic acid (C₂H₄O₂ – AcOH, Merck, 100%) and 1,3 propanediol (C₃H₈O₂, Aldrich, 98%) were used as solvents²⁵. Bismuth nitrate and iron acetylacetonate were dissolved in a mixture of glacial acetic acid and 1,3 propanediol (4:1 vol. ratio) separately room temperature. Individual solutions were poured into a beaker and stirred for 12 h to form a solution with the concentration of 0.125 M. Solutions were prepared with 5 mol% of Bi(III) excess. Precursor solutions were deposited onto Pt/TiO₂/SiO₂/(100)Si and IrO₂/TiO₂/SiO₂/(100)Si (Inostek Inc) and LNO coated Pt/TiO₂/SiO₂/(100)Si, cleaned in acetone (CH₃COCH₃, Panreac) and in 2-propanol (CH₃CHOHCH₃, Panreac, for analysis). The deposition of the BFO thin films was carried out by spin-coating at 2500 rpm for 45 s. Wet films were dried and pyrolysed on a hot-plate (IKA C-MAG HS7) at 350 °C for 1 min, followed by rapid thermal processing at 500 °C for 1 min. Deposition, drying and annealing was repeated 10 times to fabricate films with the desired thicknesses.

A grazing incidence (2°) X-ray diffraction (XRD, GIXRD, PANalytical X'Pert Pro diffractometer, Cu-K α radiation, 45 kV and 40 mA, 10° to 50° 2 θ , step size 0.025°;) was used to assess the phase assemblage and crystal structure. Residual stress analysis was carried out by XRD using sin2 ψ method²⁶ which is based shifts in the diffraction angle ($\Delta\theta$) due to changes in the inter-planar spacing, Δd . A number of XRD traces were made at different Psi (ψ) tilts. Interplanar spacing is plotted in a d vs sin2 ψ plot. Assuming a zero stress at $d = d_n$, where d is the y-intercept, stress is given by:

$$\sigma_{\phi} = \left(\frac{E}{1 + \nu} \right) m \quad (1)$$

where m is the gradient of the d vs sin2 ψ plot. The stress value for each film is obtained by substituting $E = 133$ GPa and $\nu = 0.25$ ²⁷. Using this method, we assume the films are isotropic, and stresses normal to the substrate are zero.

The microstructure of the thin films was observed at low resolution using an Hitachi SU-70 scanning electron microscope (SEM). Specimens for TEM were prepared by a gallium focused ion beam (FIB) using Helios 450S (FEI). Bright-field (BF) and dark-field (DF) TEM images were taken using a JEOL, 2200FS electron microscope at 200 kV. High-resolution (HR) TEM and ADF micrographs were obtained on Titan 200 kV ChemiStem (FEI). Energy dispersive X-ray (EDX) spectroscopy was performed using the Oxford INCA Energy TEM 250 spectrometer.

Results and discussion

Figure 1 shows the XRD traces of BFO/Pt, BFO/LNO and BFO/IrO₂ films. All peaks for BFO/IrO₂, BFO/LNO may be indexed according to either the electrode or a rhombohedrally distorted perovskite phase with R3c symmetry^{25, 28} with no evidence of any second phase. In addition to perovskite and electrode peaks, films prepared on Pt, exhibited a weak broad peak at $2\theta \sim 28.2^\circ$ (marked with an asterisk in Figure 1, attributed to a low volume fraction of a nanocrystalline Bi₂Fe₄O₉ (JCPDS PDF #01-080-8638) phase.

To study the phase formation on each type of bottom electrode, BFO films were deposited on a) Pt, b) LNO, and c) IrO₂ and annealed at 500 °C for periods of 1, 2 and 3 s with a heating rate of 100 °C/s, and 1, 5 and 30 s with a heating rate of 30 °C/s. BFO/Pt films (Figure 2a) were initially amorphous (1 s, 100 °C/s) as indicated by the presence of the broad hump centered at $2\theta \sim 29^\circ$ but as annealing time increased to 3 s (100 °C/s), they began to crystallize into perovskite BFO with complete conversion at longer times. In BFO films deposited on LNO and IrO₂, an intermediate Bi₂O₂(CO₃) phase was detected at $2\theta \sim 12.9$ and 30.3° . Bi₂O₂(CO₃) is a mineral with a tetragonal structure ($a=b=3.867$ Å and $c=13.686$ Å) and space group I4/mmm (JCPDS PDF #04-017-6012). Sun et al. identified Bi₂O₂(CO₃) as an initial phase which nucleates at pre-existing metal-organic clusters in amorphous films prepared on an electron-transparent SiN_x membrane by sol-gel²⁹.

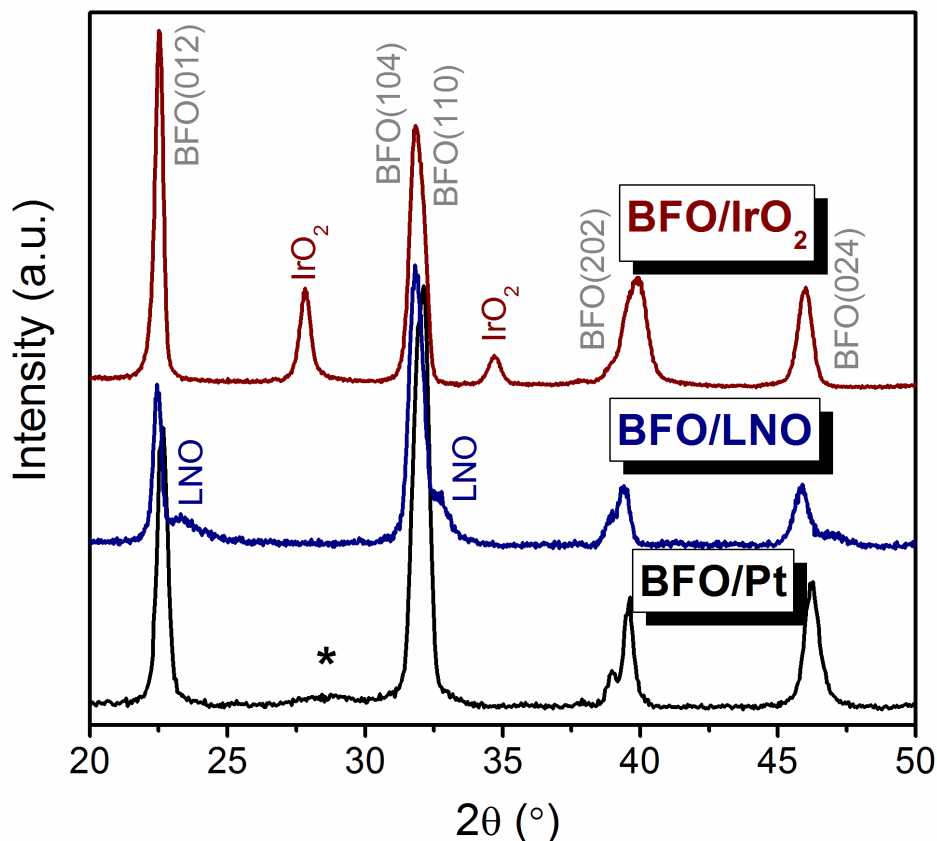
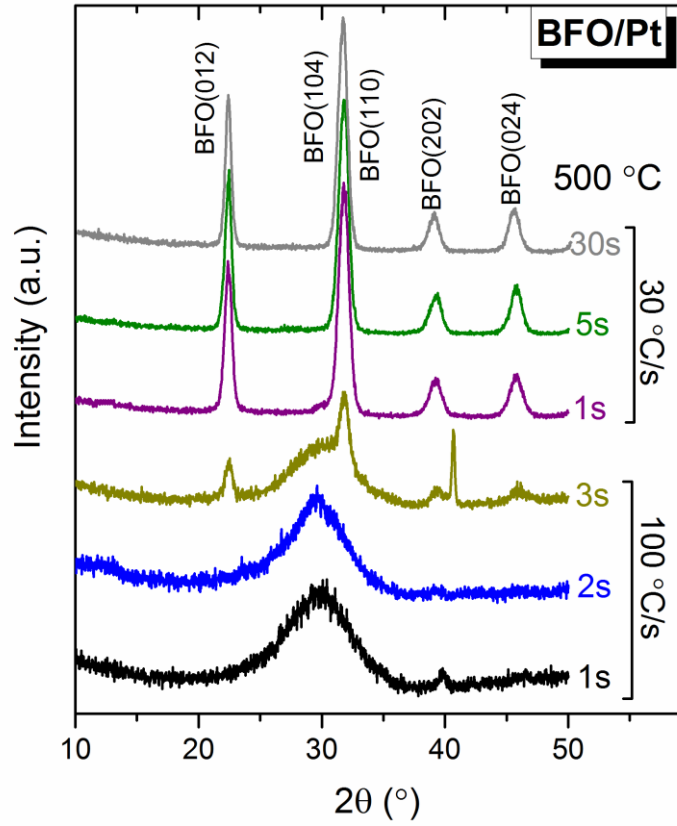
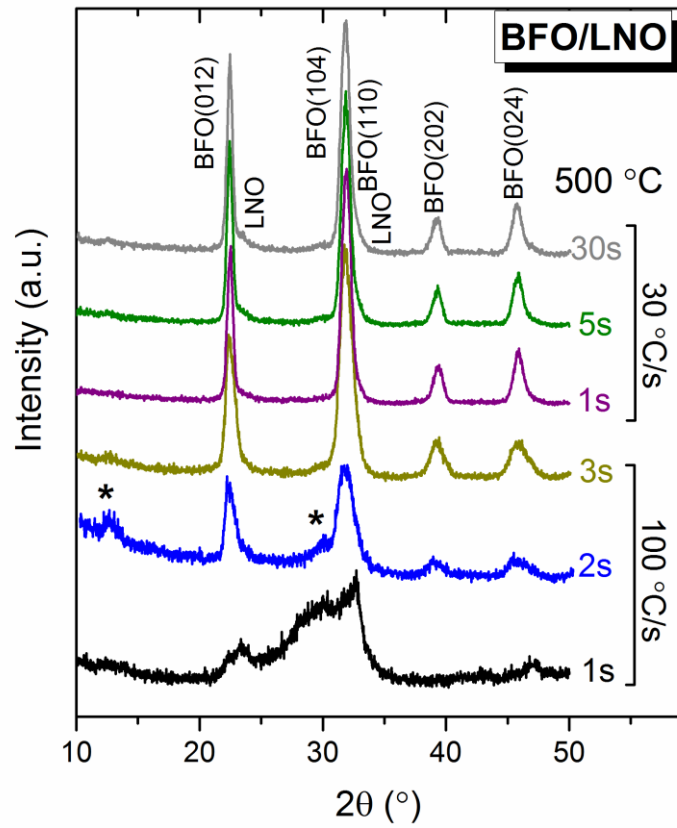


Figure 1. X-ray diffraction traces of BFO films fabricated by chemical solution deposition on Pt/Si (BFO/Pt), LNO/Pt/Si (BFO/LNO) and IrO₂/Si (BFO/IrO₂) and annealed at 500 °C. All peaks associated with BFO/IrO₂ and BFO/LNO may be attributed either to the electrode or a BFO perovskite phase whereas BFO/Pt also exhibits a weak, broad peak attributed to Bi₂Fe₄O₉(*).

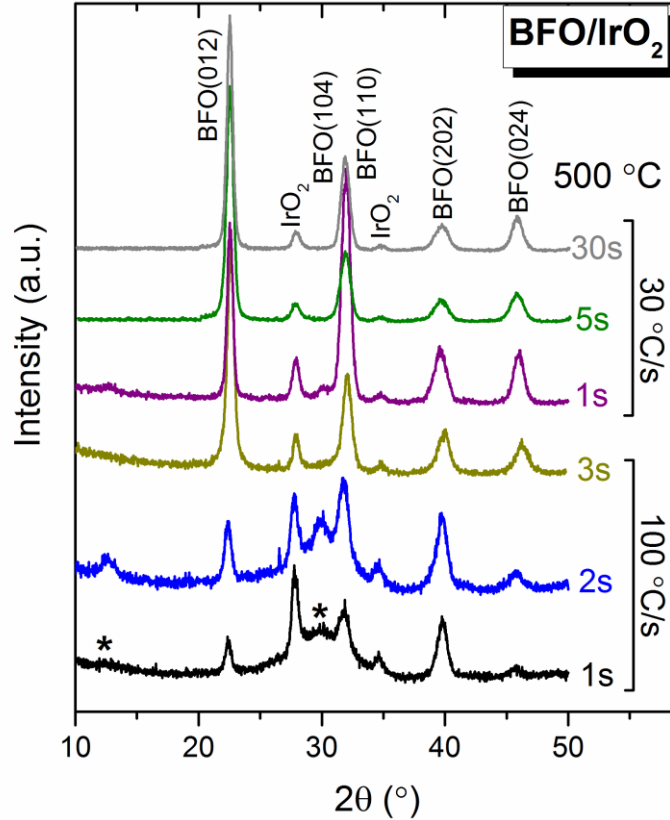
The crystallization of BFO films deposited on the oxide electrodes (Figure 2b) and c)) appears to follow the same sequence: amorphous → Bi₂O₂(CO₃) → perovskite. However, the conversion to perovskite occurs more rapidly on IrO₂ than LNO. Perovskite peaks appear after 1 s (100 °C/s) for BFO/IrO₂ but only after 2 s (100 °C/s) for BFO/LNO. It is proposed that the relatively slow amorphous to perovskite conversion for BFO/Pt allows a longer time for Bi volatilization since the vapour pressure of Bi₂O₃ above an amorphous phase is higher than that above an equivalent crystalline composition, similar to PbO above PZT³⁰. As a consequence, BFO films on Pt may be Bi deficient despite 5 % excess added to the precursor solution. This results in the presence of broad peaks in XRD traces arising from Bi deficient phases, Figure 1.



a)



b)



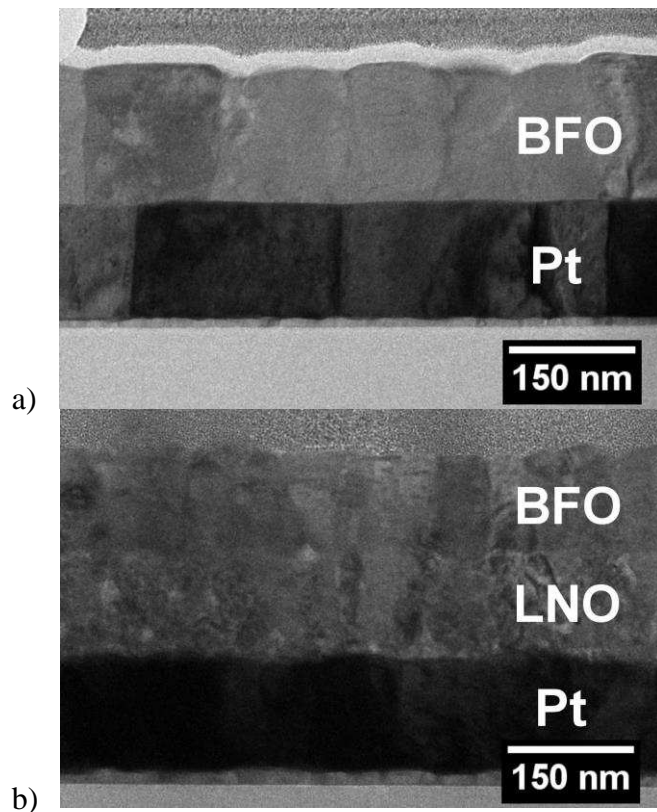
c)

Figure 2. XRD patterns of BFO thin films annealed at 500 °C for different times using heating rates of 30 and 100 °C/s. a) BFO/Pt, b) BFO/LNO, and c) BFO/IrO₂. * denotes Bi₂O₂(CO₃).

Figure 3 shows images of cross-sections of BFO/LNO, BFO/Pt and BFO/IrO₂ thin films. The thickness of BFO layers measured from TEM images is 150, 170 and 200 nm with a columnar microstructure in each case with lateral grain size, 80, 140 and 200 nm for BFO/LNO, BFO/Pt and BFO/IrO₂, respectively. The smallest grain size of BFO/LNO indicates that BFO has lower nucleation barrier while deposited on LNO comparing to Pt and IrO₂ due to the same crystal structure and small lattice mismatch, ~3 %. In such case, the large density of formed nuclei leads to a development of smaller grain size. In the case of BFO/Pt and BFO/IrO₂ much fewer nuclei are formed, thus they grow into much larger grains. The columnar grains extend through the entire film thickness which indicates layer-by-layer homoepitaxy for BFO growth within a grain³¹. As discussed in the literature, crystallization of solution-based films is characterized by competition between bulk nucleation within the amorphous matrix, and heterogeneous

nucleation at the interfaces³¹. Columnar grain growth in thin films can only be achieved if interface nucleation is favoured over bulk nucleation³¹. Low solution concentration and the thermal treatment conditions at which each layer is crystallized before the next layer is deposited, promotes interfacial nucleation and columnar grain growth. For SrTiO₃ and BaTiO₃ films, depositing thin layers (10-20 nm) and annealing induces nucleation at the interfaces between the layers and encourages local epitaxial growth³². In this study, 10 layers were spin coated onto the substrates, dried and annealed at 500 °C, leading to columnar grain growth with layer thicknesses of 12-18 nm, as deduced from TEM images in Figure 3.

In addition to the individual layers, Figure 3 revealed inclusions of bright contrast in the interior of the BFO grains, often between the deposited layers. This contrast could arise due to the segregation of light elements, the formation secondary phase with high quantity of lighter elements, or the formation of pores. Porosity has been previously reported in sol-gel processed 0.9PMN-0.1PT thin films and attributed to fast crystallization³³.



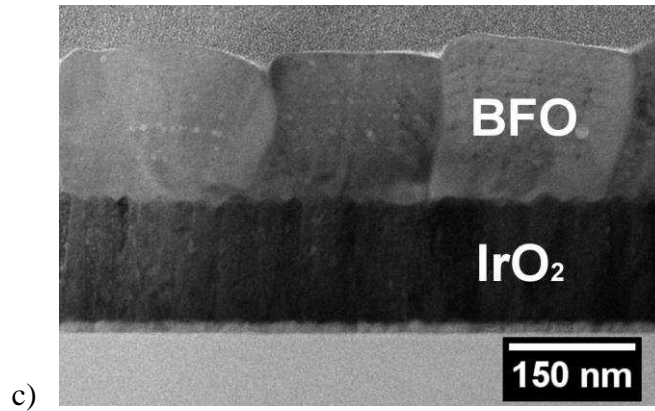


Figure 3 Bright-field TEM images of cross-sections of a) BFO/Pt, b) BFO/LNO and c) BFO/IrO₂ thin films showing a columnar grain structure. The average width of the columnar grains is 80, 140 and 200 nm for BFO/LNO, BFO/Pt and BFO/IrO₂, respectively.

Figure 4 however, presents higher magnification annular dark field (ADF) images in which the brightness at each atomic position is approximately proportional to the square of atomic number (Z)³⁴. Therefore, the bright areas in Figure 3 correspond to scattering from Bi atoms with the highest Z and the darkest to Fe atoms with lower Z . The bright contrast inclusions in Figure 4 exhibit dark contrast in the ADF images, indicating that these regions are deficient in Bi compared with the neighboring bright contrast areas. For BFO on IrO₂, the precipitates are <10 nm and generally located away from the grain boundaries, Figure 4c. For BFO films on LNO, larger inclusions (10-15 nm) are present within the film interior, whereas smaller inclusions (5nm) exist at the interfaces between the crystallization layers (Figure 4b). For BFO on Pt, small inclusions (10 nm) are present in the grain interior but larger elongated inclusions with dark contrast occur at the grain boundaries, Figure 4a.

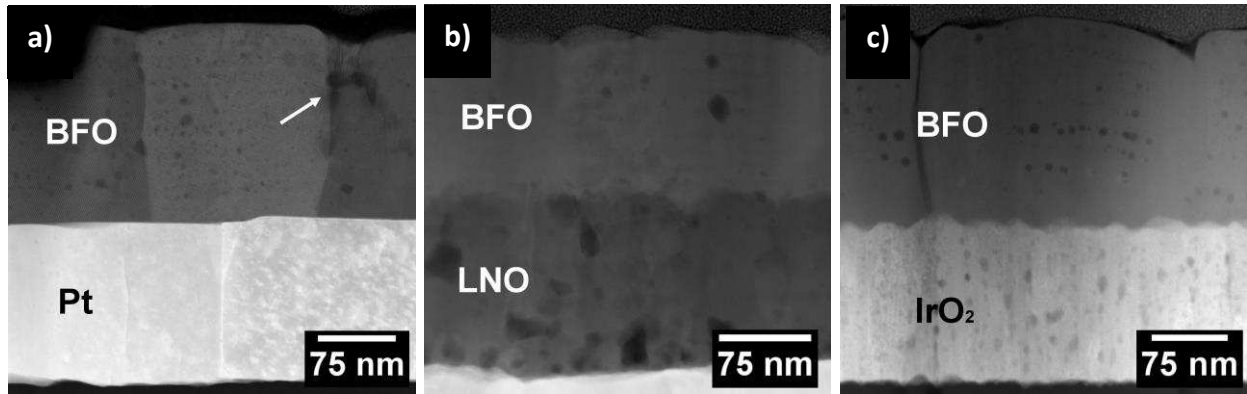


Figure 4. ADF TEM cross-sectional micrographs of the a) BFO/Pt, b) BFO/LNO and c) BiFeO₃/IrO₂ thin films. A grain boundary with second phase (indicated by the arrowhead) is shown in Figure 4a. Inclusions inside the columnar grains exhibit dark contrast in ADF images, indicating that these regions are poor in heavier elements compared with the bright contrast in neighboring areas.

To clarify the chemical composition of the grain boundary secondary phase in BFO on Pt, EDX line-scans were performed, as denoted by the white line in Figure 5a, with the traces inset. The line-scans reveal that the particles are poor in Bi and rich in Fe with respect to the matrix, corroborating the XRD data (Figure 1) and ADF images (Figure 4) which suggests the presence Bi deficient phases. High resolution images (Figure 5b) reveal lattice fringes with a measured spacing of 0.552 nm, consistent with d_{110} (0.579 nm) of orthorhombic Bi₂Fe₄O₉ (JCPDS PDF #01-080-8638).

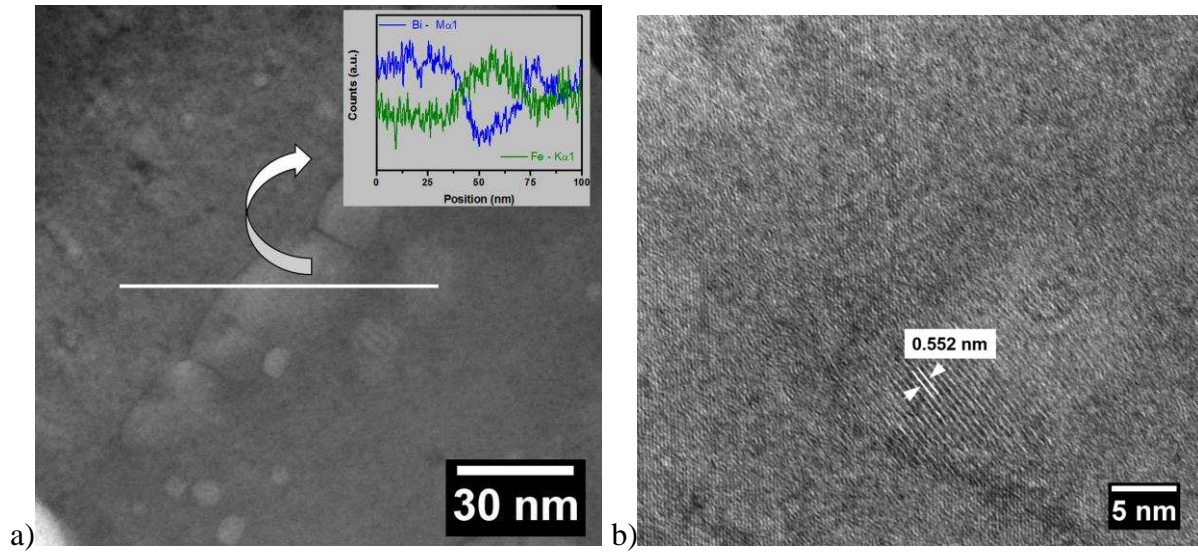


Figure 5. a) STEM micrographs of second phase at the grain boundary of a BFO/Pt thin film with inset line-scan EDX plots obtained along the white line. The grain boundary phase is poor in Bi and rich in Fe with respect to the matrix, b) high resolution lattice image of a second phase, grain boundary particle whose d-spacings are consistent with d_{110} (0.579 nm) $\text{Bi}_2\text{Fe}_4\text{O}_9$ phase.

In contrast, high resolution images of the grain interior (Figure 6a) illustrate that the small inclusions are fully coherent with the matrix, despite being Fe rich according to the contrast within ADF images, Figure 4. Their location, primarily at the layer interfaces, suggests that their occurrence relates to Bi loss at the surface of each individual layer, the mechanism for which is illustrated in Figure 6b. The high surface/volume ratio of thin films make them prone to Bi loss. In layer by layer deposition used in this study, the perovskite crystals in lower are nucleation sites for those in upper layers and grains transmit their orientation, leading to columnar growth. The precipitates do not disrupt this epitaxial nucleation process, consistent with the notion that they are fully coherent.

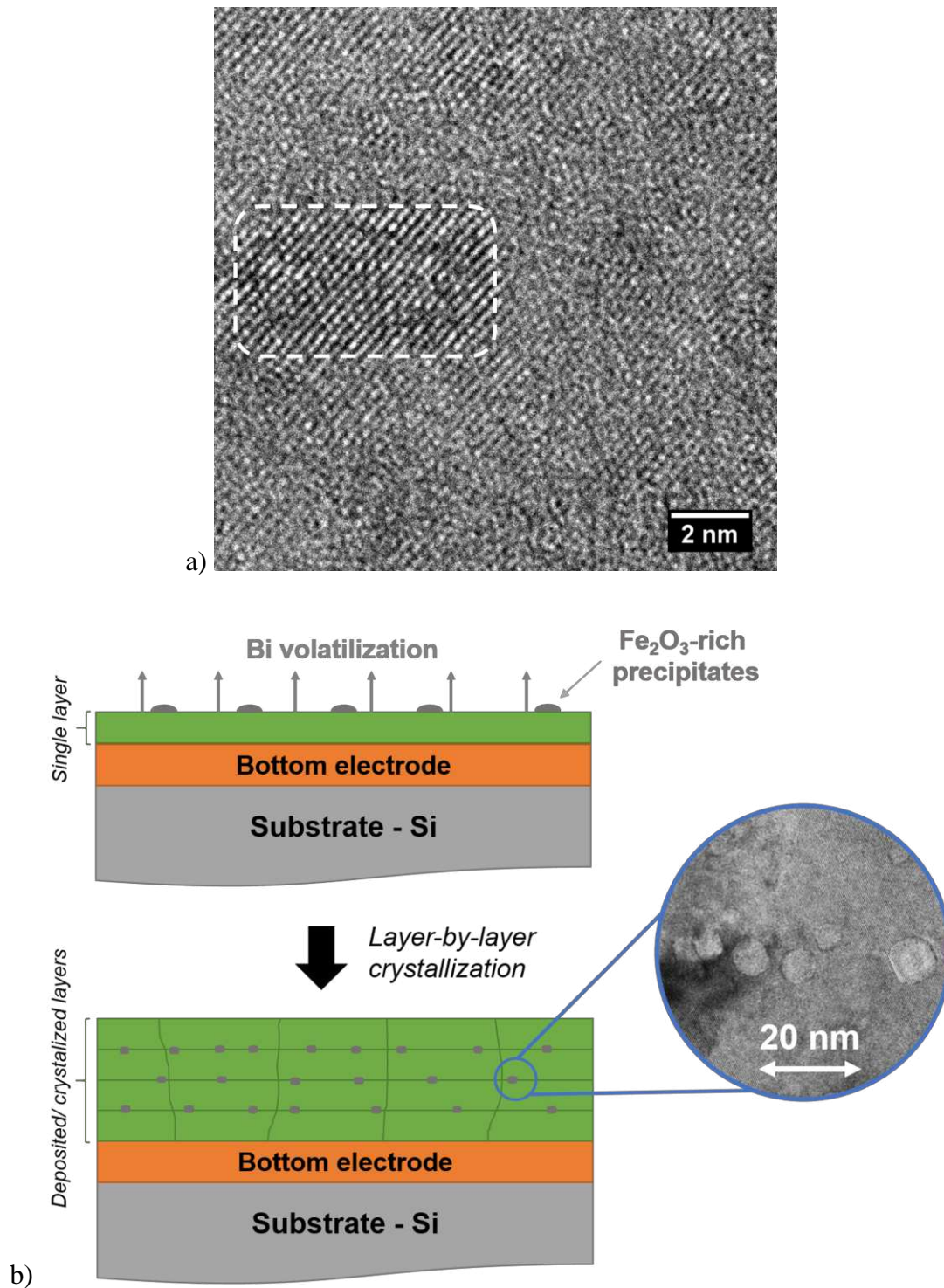


Figure 6. a) HRTEM micrograph of the inclusion in the grain interior which indicates that they are coherent (marked by dashed line) and b) proposed mechanism of inclusion formation (with bright-field TEM micrograph embedded).

During the preparation of Bi-containing films, problems relating to interdiffusion and chemical fluctuations have been previously reported³⁵. Yakovlev et al. using XPS analysis, showed a wide film–electrode interface reaction due to interdiffusion in BFO films grown on Pt/Si substrates, pointing to the formation of Pt–Bi and Pt–Fe intermetallic compounds at the bottom electrode–film interface³⁵. High-magnification ADF images of BFO/Pt, BFO/LNO and BFO/IrO₂ interfaces are shown in Figure 7. The BFO/Pt interface (Figure 7a) appears sharp with the Pt relatively flat compared to IrO₂ and LNO. Figure 7b shows that the BFO/LNO interface is broadened by the slight curvature of the grain boundaries of LNO. Figure 7c reveals that the BFO/IrO₂ interface is not flat but consists of a series of roughly curved boundaries reflecting the topography of columnar grains of IrO₂. Experimental and theoretical studies have demonstrated that the interface roughness has a great influence on the electrical properties of dielectric films, especially leakage current³⁶. All interfaces between BFO films and electrodes are free from interaction layers and secondary phases.

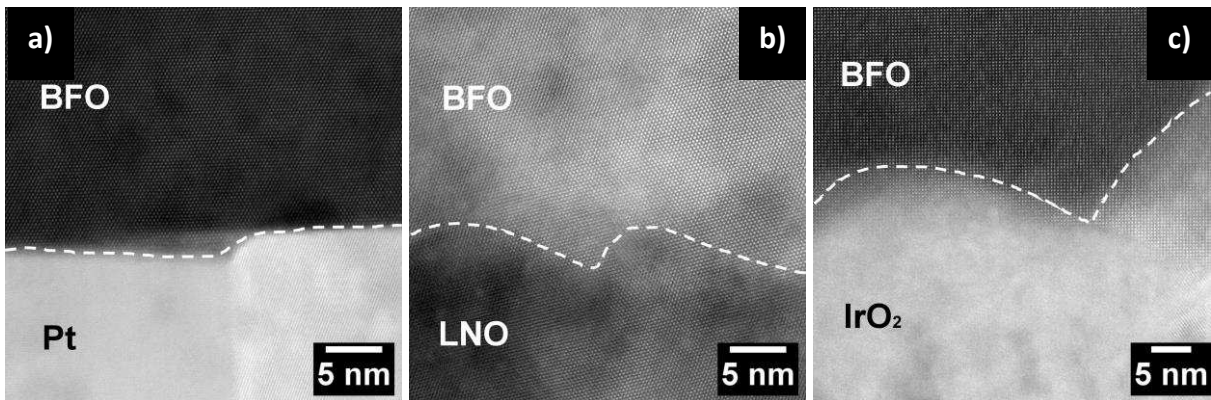


Figure 7. ADF TEM micrographs of a) BFO/Pt, b) BFO/LNO and c) BFO/IrO₂ interfaces (marked by dashed line). No secondary phase was detected at the interface between BFO and bottom electrodes.

The effect that the bottom electrode has on residual stress in BFO films was also addressed. In a film, the total residual stress consists of: i) intrinsic stress induced by the formation of the grain boundaries during the crystal grain growth; ii) thermal stress due to the difference between thermal expansion coefficients of the film and the substrate and iii) extrinsic stress that originates

from the lattice parameter mismatch³⁷. The average residual stresses calculated by XRD $\sin^2\psi$ method are 0.72, 0.49 and 0.77 GPa for BFO/Pt, BFO/LNO and BFO/IrO₂, respectively, as presented in Figure 8. The stresses are tensile in all cases. Thermal stress and extrinsic stress are strongly related to the parameters listed in the embedded table in Figure 8. Based on the difference in thermal expansion coefficient between BFO and Si, tensile thermal stress in BFO films is expected, although the effect of bottom electrode (Pt, IrO₂, LNO) on BFO residual stress cannot be ignored. On the other hand, the lattice parameter mismatch is the smallest between BFO and Pt however only BFO and LNO holds the same crystallographic structure (rhombohedral perovskite) that can be responsible for the lowered residual stress in BFO/LNO. Moreover, grain growth can substantially contribute to tensile stresses in a constrained film through elimination of the excess volume associated with grain boundaries and grain size has a dominant impact on the residual stress^{38, 39}. Indeed, in our BFO thin films residual stress decreases with decreasing grain size. The highest residual stress was observed for BFO/IrO₂ film which has the largest grain size. In contrast, the stress state in BFO/LNO is lowered due a smaller lateral grain size.

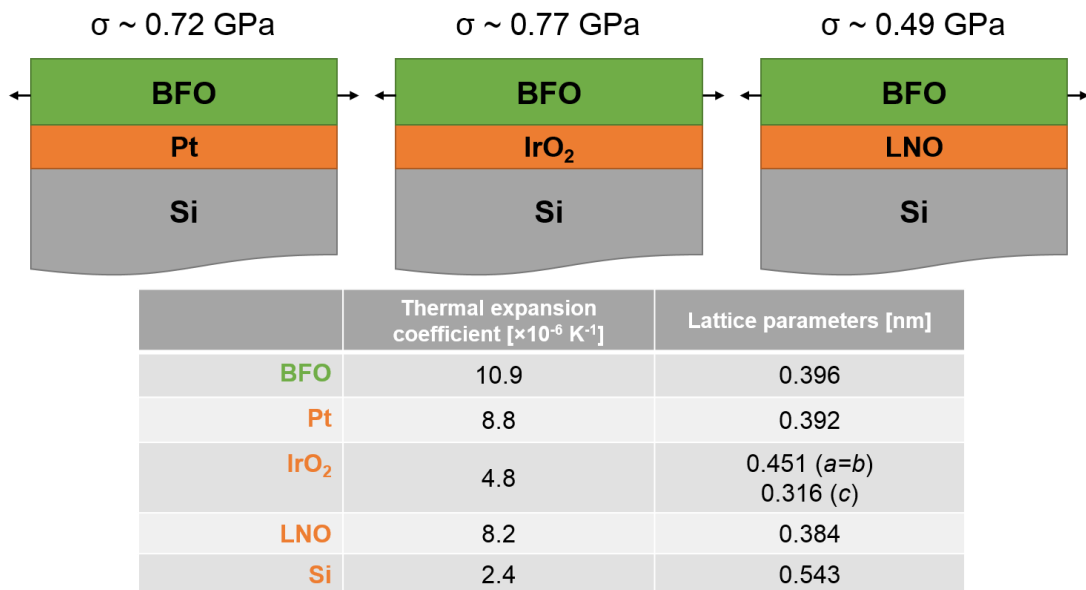


Figure 8. Schematic illustrating the average residual stresses calculated by XRD $\sin^2\psi$ method for BFO films on distinct electrodes. The lattice and thermal expansion coefficient of the BFO

and bottom electrode materials were listed⁴⁰⁻⁴². The stresses are tensile in all cases. The highest residual stress was observed for BFO/IrO₂ and the lowest in BFO/LNO thin films.

Figure 9 is a dark-field image of one of the columnar grains in a BFO films on LNO. This grain has an epitaxial relationship with a grain in the LNO layer. In contrast, films grown on Pt and IrO₂ did not exhibit an epitaxial orientation relationship with the electrode. Unlike IrO₂ and Pt, LNO has the perovskite structure with lattice parameter $a = 0.384$ nm, compatible with that of BFO, $a = 0.396$ nm and thus epitaxy is more likely⁴³ and may contribute to lowering of residual stress.

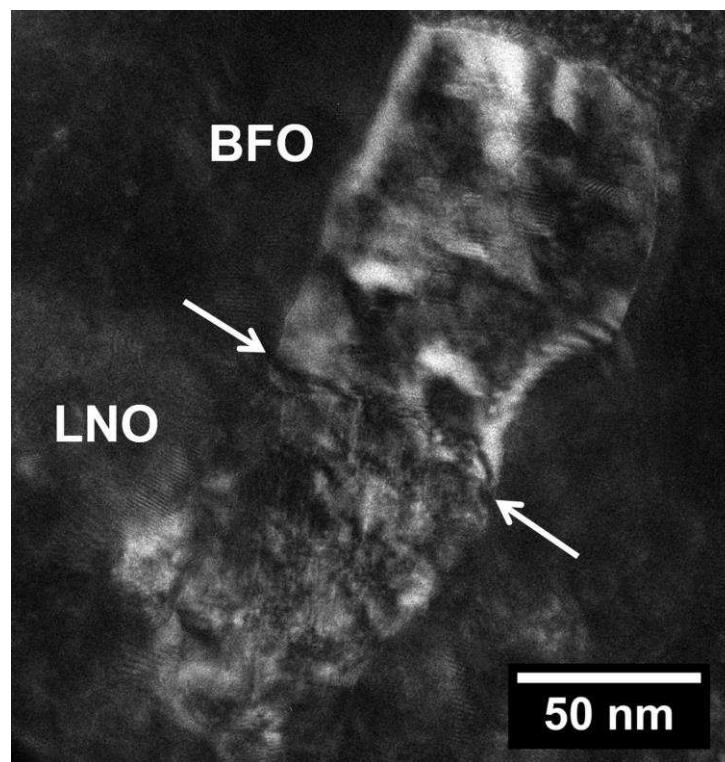


Figure 9. Dark-field image of a columnar grain in the BFO film on LNO. Local epitaxial growth of BFO on LNO was observed.

Conclusions

In summary, ADF imaging, STEM, HRTEM and EDX complemented with grazing incident XRD were used to analyze the microstructure and phase formation of BFO thin films prepared by the chemical solution deposition on Pt/TiO₂/SiO₂/(100)Si, LNO/Pt/TiO₂/SiO₂/(100)Si and IrO₂/TiO₂/SiO₂/(100)Si substrates. All the BFO films showed a columnar structure with the grain size depending on the bottom electrode. Formation of Bi₂Fe₄O₉ was observed at the grain boundaries of BFO/Pt but coherent Fe-rich precipitates were observed in the grain interior for all studied films. The crystallization of BFO films deposited on the oxide electrodes followed the sequence: amorphous → Bi₂O₂(CO₃) → perovskite, while BFO on Pt crystallized directly from amorphous phase. IrO₂ was the most effective at promoting transformation to perovskite whilst LNO induced local epitaxial growth. Residual stress analysis of BFO films revealed that they are subject to tensile stress whose magnitude depends on the bottom electrode.

Acknowledgments

This work was developed within the scope of the project CICECO-Aveiro Institute of Materials, POCI-01-0145-FEDER-007679 (FCT Ref. UID/CTM/50011/2013), financed by national funds through the FCT/MEC and when appropriate co-financed by FEDER under the PT2020 Partnership Agreement. Monika Tomczyk acknowledges FCT for financial support (SFRH/BD/81123/2011). Ian M. Reaney acknowledges the support of the Engineering and Physical Science Research Council Grant, EP/I038934/1.

References:

1. D. Khomskii, *Physics*, 2009, **2**, 20.
2. R. Safi and H. Shokrollahi, *Progress in Solid State Chemistry*, 2012, **40**, 6-15.
3. G. D. Achenbach, W. J. James and R. Gerson, *Journal of the American Ceramic Society*, 1967, **50**, 437-437.
4. J. R. Teague, R. Gerson and W. J. James, *Solid State Commun*, 1970, **8**, 1073-1074.

5. G. Catalan and J. F. Scott, *Advanced Materials*, 2009, **21**, 2463-2485.
6. S. M. Selbach, M.-A. Einarsrud and T. Grande, *Chemistry of Materials*, 2009, **21**, 169-173.
7. M. S. Bernardo, T. Jardiel, M. Peiteado, A. C. Caballero and M. Villegas, *Journal of the European Ceramic Society*, 2011, **31**, 3047-3053.
8. T. Rojac, A. Bencan, B. Malic, G. Tutuncu, J. L. Jones, J. E. Daniels and D. Damjanovic, *Journal of the American Ceramic Society*, 2014, **97**, 1993-2011.
9. M. Murakami, S. Fujino, S.-H. Lim, L. G. Salamanca-Riba, M. Wuttig, I. Takeuchi, B. Varughese, H. Sugaya, T. Hasegawa and S. E. Lofland, *Applied Physics Letters*, 2006, **88**, 112505.
10. H. Zhang, I. M. Reaney, D. M. Marincel, S. Trolier-McKinstry, Q. M. Ramasse, I. MacLaren, S. D. Findlay, R. D. Fraleigh, I. M. Ross, S. Hu, W. Ren and W. Mark Rainforth, *Scientific Reports*, 2015, **5**, 13066.
11. F. Tyholdt, H. Fjellvåg, A. E. Gunnæs and A. Olsen, *Journal of Applied Physics*, 2007, **102**, 074108.
12. S. Iakovlev, C.-H. Solterbeck, M. Kuhnke and M. Es-Souni, *Journal of Applied Physics*, 2005, **97**, 094901.
13. S. Singh, K., R. Ueno, H. Funakubo, H. Uchida, S. Koda and H. Ishiwara, *Japanese Journal of Applied Physics*, 2005, **44**, 8525.
14. A. Z. Simões, C. S. Riccardi, M. L. Dos Santos, F. G. Garcia, E. Longo and J. A. Varela, *Materials Research Bulletin*, 2009, **44**, 1747-1752.
15. N. Izyumskaya, Y. I. Alivov, S. J. Cho, H. Morkoç, H. Lee and Y. S. Kang, *Critical Reviews in Solid State and Materials Sciences*, 2007, **32**, 111-202.
16. C. U. Pinnow, I. Kasko, N. Nagel, T. Mikolajick, C. Dehm, F. Jahnelt, M. Seibt, U. Geyer and K. Samwer, *Journal of Applied Physics*, 2002, **91**, 1707-1709.
17. B. Nagaraj, S. Aggarwal and R. Ramesh, *Journal of Applied Physics*, 2001, **90**, 375-382.
18. A. K. Tagantsev, I. Stolichnov, E. L. Colla and N. Setter, *Journal of Applied Physics*, 2001, **90**, 1387-1402.
19. J. Xiao, A. Wu, P. M. Vilarinho, A. R. Ramos and E. Alves, *J Mater Chem*, 2009, **19**, 5572-5579.
20. K. H. Yoon, J.-H. Sohn, B. D. Lee and D. H. Kang, *Applied Physics Letters*, 2002, **81**, 5012-5014.

21. D. Sando, A. Barthélémy and M. Bibes, *Journal of Physics: Condensed Matter*, 2014, **26**, 473201.
22. Z. X. Cheng, X. L. Wang, H. Kimura, K. Ozawa and S. X. Dou, *Applied Physics Letters*, 2008, **92**, 092902.
23. Y.-H. Lee, J.-M. Wu, Y.-L. Chueh and L.-J. Chou, *Applied Physics Letters*, 2005, **87**, 172901.
24. H. Liu and X. Wang, *Journal of Alloys and Compounds*, 2009, **485**, 769-772.
25. C. Gutiérrez-Lázaro, I. Bretos, R. Jiménez, J. Ricote, H. E. Hosiny, D. Pérez-Mezcua, R. J. Jiménez Rioboó, M. García-Hernández and M. L. Calzada, *Journal of the American Ceramic Society*, 2013, **96**, 3061-3069.
26. U. Welzel, J. Ligot, P. Lamparter, A. C. Vermeulen and E. J. Mittemeijer, *Journal of Applied Crystallography*, 2005, **38**, 1-29.
27. S. Dutta, A. Pandey, O. P. Thakur, R. Pal and R. Chatterjee, *Journal of Applied Physics*, 2013, **114**, 174103.
28. A. H. M. Gonzalez, A. Z. Simões, L. S. Cavalcante, E. Longo, J. A. Varela and C. S. Riccardi, *Applied Physics Letters*, 2007, **90**, 052906.
29. T. Sun, H. Hu, Z. Pan, X. Li, J. Wang and V. P. Dravid, *Physical Review B*, 2008, **77**, 205414.
30. P. Muralt, *Journal of Applied Physics*, 2006, **100**, 051605.
31. R. W. Schwartz, T. Schneller and R. Waser, *Comptes Rendus Chimie*, 2004, **7**, 433-461.
32. R. W. Schwartz, P. G. Clem, J. A. Voigt, E. R. Byhoff, M. Van Stry, T. J. Headley and N. A. Missert, *Journal of the American Ceramic Society*, 1999, **82**, 2359-2367.
33. Y. Bastani and N. Bassiri-Gharb, *Journal of the American Ceramic Society*, 2012, **95**, 1269-1275.
34. D. G. Stroppa, L. F. Zagonel, L. A. Montoro, E. R. Leite and A. J. Ramirez, *ChemPhysChem*, 2012, **13**, 437-443.
35. S. Yakovlev, J. Zekonyte, C. H. Solterbeck and M. Es-Souni, *Thin Solid Films*, 2005, **493**, 24-29.
36. Y. P. Zhao, G. C. Wang, T. M. Lu, G. Palasantzas and J. T. M. De Hosson, *Physical Review B*, 1999, **60**, 9157-9164.

37. K. K. Maurya, S. K. Halder, S. Sen, A. Bose and S. Bysakh, *Applied Surface Science*, 2014, **313**, 196-206.
38. F. Spaepen, *Acta Materialia*, 2000, **48**, 31-42.
39. S. Lu, C. Zuo, H. Zeng, W. Huang and H. Ji, *Mater Lett*, 2006, **60**, 255-260.
40. G. Bayer and H. G. Wiedemann, *Thermochimica Acta*, 1975, **11**, 79-88.
41. B. H. Kim, J. H. An and K. S. Hwang, *J Mater Sci*, 2006, **41**, 2165-2166.
42. S. K. Singh, H. Ishiwara and K. Maruyama, *Journal of Applied Physics*, 2006, **100**, 064102.
43. Y. Wang, Y. Lin and C.-W. Nan, *Journal of Applied Physics*, 2008, **104**, 123912.

Figure Captions:

Figure 1. X-ray diffraction traces of BFO films fabricated by chemical solution deposition on (a) Pt/Si (BFO/Pt), (b) LNO/Pt/Si (BFO/LNO) and (c) IrO₂/Si (BFO/IrO₂) and annealed at 500 °C. All peaks associated with BFO/IrO₂ and BFO/LNO may be attributed either to the electrode or a BFO perovskite phase whereas BFO/Pt also exhibits a weak, broad peak attributed to Bi₂Fe₄O₉(*).

Figure 2. XRD patterns of BFO thin films annealed at 500 °C for different times using heating rates of 30 and 100 °C/s. a) BFO/Pt, b) BFO/LNO, and c) BFO/IrO₂. * denotes Bi₂O₂(CO₃).

Figure 3 Bright-field TEM images of cross-sections of a) BFO/Pt, b) BFO/LNO and c) BFO/IrO₂ thin films showing a columnar grain structure. The average width of the columnar grains is 80, 140 and 200 nm for BFO/LNO, BFO/Pt and BFO/IrO₂, respectively.

Figure 4. ADF TEM cross-sectional micrographs of the a) BFO/Pt, b) BFO/LNO and c) BiFeO₃/IrO₂ thin films. A grain boundary with second phase (indicated by the arrowhead) is shown in Figure 3a. Inclusions inside the columnar grains exhibit dark contrast in ADF images, indicating that these regions are poor in heavier elements compared with the bright contrast in neighboring areas.

Figure 5. a) STEM micrographs of second phase at the grain boundary of a BFO/Pt thin film with inset line-scan EDX plots obtained along the white line. The grain boundary phase is poor in Bi and rich in Fe with respect to the matrix, b) high resolution lattice image of a second phase, grain boundary particle whose d-spacings are consistent with d₁₁₀ (0.579 nm) Bi₂Fe₄O₉ phase.

Figure 6. a) HRTEM micrograph of the inclusion in the grain interior which indicates that they are coherent (marked by dashed line) and b) proposed mechanism of inclusion formation (with bright-field TEM micrograph embedded).

Figure 7. ADF TEM micrographs of a) BFO/Pt, b) BFO/LNO and c) BFO/IrO₂ interfaces (marked by dashed line). No secondary phase was detected at the interface between BFO and bottom electrodes.

Figure 8. Schematic illustrating the average residual stresses calculated by XRD $\sin^2\psi$ method for BFO films on distinct electrodes. The lattice and thermal expansion coefficient of the BFO and bottom electrode materials were listed⁴⁰⁻⁴². The stresses are tensile in all cases. The highest residual stress was observed for BFO/ IrO_2 and the lowest in BFO/LNO thin films.

Figure 9. Dark-field image of a columnar grain in the BFO film on LNO. Local epitaxial growth of BFO on LNO was observed.